4. Graphite: Strongly Coupled Optical Phonons in Action

In this chapter, TRTS is applied to the semimetal graphite. The raw data, the extraction of the dielectric function, and the fit to models based on the extremely well-developed theory of the electronic structure of graphite around the Fermi level are described in detail. This yields the temporal evolution of the electronic temperature, the plasma frequency, and the Drude scattering rate. Simple physical arguments and model calculations show that more than 90 % of the initially deposited excitation energy is transferred to only few strongly coupled lattice vibrations within less 500 fs. These hot optical phonons also substantially contribute to the striking increase of the Drude relaxation rate observed during the first ps after photoexcitation. The subsequent cooling of the hot phonons yields a lifetime estimate of 5.4 ps for these modes.

Parts of this chapter have been published in Physical Review Letters ***95****, 187403 (2005).*

4.1. Motivation

The textbook-like semimetal graphite has been studied for more than 6 decades due to its relatively simple quasi-2-dimensional structure [Dre88]. For example, it was among the first materials for which the electronic band structure was calculated [Wal47]. Despite this long history, graphite still attracts continuous attention in research as illustrated by the following examples:

- As shown in Fig. 4.1, thin graphite films exhibit a strong electric-field effect which demonstrates their potential for nanoelectronics: Due to the higher charge carrier density, they permit much higher current densities and shorter screening lengths than doped semiconductors and may lead to the construction of smaller and faster devices [Nov04].

- Graphite serves as a model system for metallic carbon nanotubes, particularly in terms of electrons around the Fermi edge and optical phonons which strongly couple to the electrons [Pis04, Mau04]. These phonons have quantum energies of up to 0.2 eV and are believed to decrease the dc conductivity of carbon nanotubes when high electric fields are applied [Jav04].

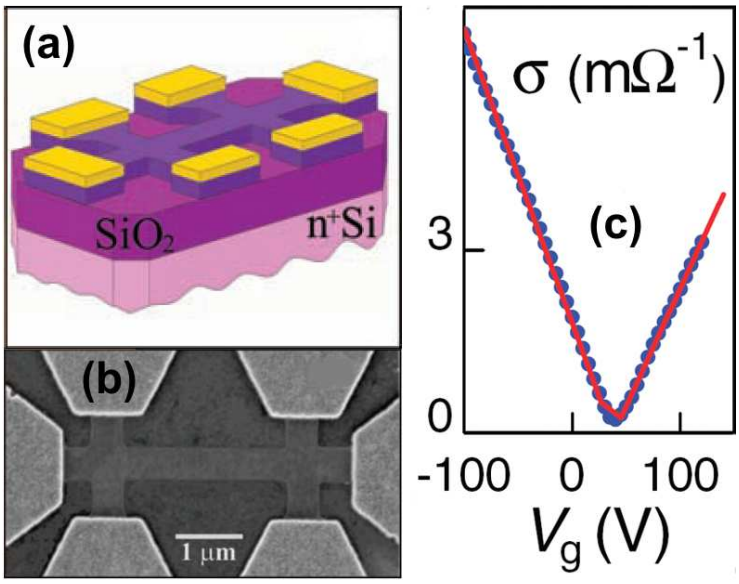

Figure 4.1.: Electric-field effect in thin graphite films, taken from Ref. [Nov04]. (a) Schematic of the field-effect device. It consists of a graphite film fixed to a Si substrate with the bottom side and contacted by gold electrodes from the top. The gate voltage is applied between a gold contact and the n-doped Si substrate. (b) Picture of the device taken by scanning electron microscopy. (c) Conductivity σ versus gate voltage V_g. The graph demonstrates that the device can switch between the conducting and non-conducting state.

In view of possible applications in electronics, further investigations are required on how the strongly coupled optical phonons (SCOPs) influence the transport and energy relaxation of electrons. Time-resolved THz spectroscopy (TRTS) is a promising experimental approach to this question. A visible pump pulse excites charge carriers in the sample and thus enables them to emit optical phonons. A subsequent THz pulse probes the electrons around the Fermi edge.

In addition, TRTS has never been applied to a semimetal. Before presenting the experimental results, some basics of graphite are summarized.

4.2. General Properties

Graphite is, like diamond, one of the modifications of carbon (C). The 4 valence electrons of a C atom can produce a great variety of chemical bonds which strongly influence the properties of the resulting material [Hak03]. In graphite, each C atom is sp^2 hybridized and the center of 3 covalent σ and π bonds to other C atoms. These atoms are arranged on a honeycomb lattice and form a sheet of so-called graphene. Van der Waals forces lead to weaker and longer bonds between adjacent graphene sheets and to the typical layered structure which is illustrated in Fig. 4.2(a). Figures 4.2(b,c) show that the ABAB... stacking sequence results in a hexagonal close packed (hcp) lattice structure with 4 carbon atoms in the unit cell.

The distance $c_0/2 = 3.35\,\text{Å}$ of 2 adjacent graphene layers is significantly longer than the σ-bond length of 1.42 Å [Hol92]. The layered structure of graphite implies a corresponding pronounced anisotropy in macroscopic properties such as electric conductivity, optical response and elasticity.

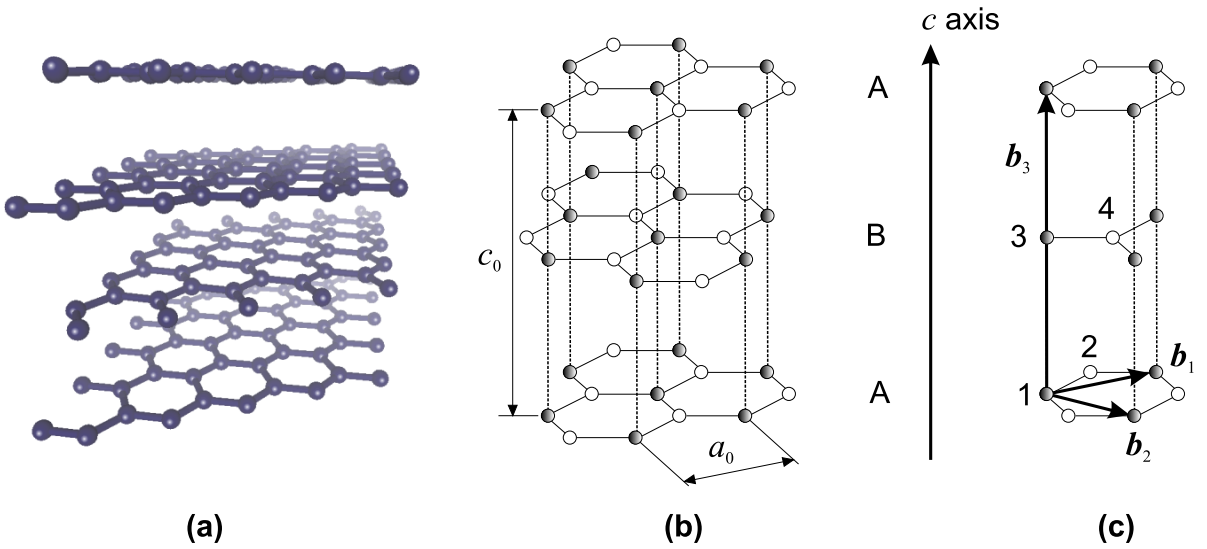

Figure 4.2.: (a) Schematic of the graphite lattice which is a stack of honeycomb meshes of C atoms. A single mesh is also called a graphene sheet. (b) Magnified section of the graphite lattice together with lattice constants $a_0 = 2.46\,\text{Å}$ and $c_0 = 6.71\,\text{Å}$. The graphene layers are stacked in an ABAB... sequence. (c) Possible hexagonal elementary cell containing the 4 atoms 1, 2, 3, and 4. Lattice basis vectors $\boldsymbol{b}_1$, $\boldsymbol{b}_2$, and $\boldsymbol{b}_3$ are also shown where $\boldsymbol{b}_3$ is parallel to the c axis. One has $|\boldsymbol{b}_1| = |\boldsymbol{b}_2| = a_0$ and $|\boldsymbol{b}_3| = c_0$. Parts of this figure were taken from [Hag05a].

4.2.1. Highly Oriented Pyrolytic Graphite

Synthetic graphite is produced by pyrolysis where gaseous hydrocarbons are thermally cracked. The resulting carbon gas covers a substrate in layer-by-layer growth while a substrate temperature of more than 2500 °C induces the sp^2 hybridization of the C atoms. The subsequent application of high pressures and temperatures results in so-called highly oriented pyrolytic graphite (HOPG) which is the material investigated in this chapter.

HOPG consists of graphite crystallites with linear dimensions of a few 10 μm perpendicular and a few 10 nm parallel to the c axis [Ohl97]. All crystallites have their c axes in the same direction but are rotated around their individual c axis randomly.

4.3. Electronic Structure

In order to analyze the data presented in this chapter, knowledge on the electronic structure of graphite around the Fermi edge is required. The graphene model of the graphite band structure is sufficient for a qualitative argumentation whereas the more sophisticated model of Slonczewski, Weiss, and McClure (SWM) is used for the numerical simulations.

4.3.1. Graphene: Tight-Binding Model

In a first approach, the interaction between the graphite layers is neglected. It is then sufficient to consider only 1 graphene sheet. The sp^2 hybridization of the 2s and the $2p_x$, $2p_y$ and $2p_z$ orbitals leads to three sp^2 orbitals and one p_z orbital for the 4 valence electrons of a C atom where the z axis is perpendicular to the graphene sheet.

A σ bond between 2 adjacent C atoms is due to their well overlapping sp^2 orbitals and lowers the energy of the 2 participating electrons. The π bond is much weaker due to the smaller overlap of the p_z orbitals and, therefore, contains the electrons with the lowest excitation energies. For this reason, the bonding π and antibonding π^* states mainly determine the electronic structure of graphite within a few eV around the Fermi energy.

In addition, the small overlap of the wavefunctions in a π bond does not significantly alter the p_z wavefunctions of the isolated atoms. Therefore, a tight-binding approach for the calculation of the band structure is promising in which the Bloch states are approximated by linear combinations of the p_z orbitals. Since the graphene unit cell contains two C atoms and since only 1 basis orbital is involved, solving the stationary Schrödinger equation yields 2 electronic bands [Dre88]

$$\left.\begin{matrix}\epsilon_{\boldsymbol{k}\pi^*}\\ \epsilon_{\boldsymbol{k}\pi}\end{matrix}\right\} = \pm\frac{\gamma_0 w(\boldsymbol{k})}{1 \mp s w(\boldsymbol{k})} \tag{4.1}$$

with

$$w(\boldsymbol{k}) = \sqrt{1 + 4\cos^2(k_y a_0/2) + 4\cos(\sqrt{3}k_x a_0/2)\cos(k_y a_0/2)}$$

which originate from the bonding π and antibonding π^* states. As expected, the band structure depends only on the wavevectors $\boldsymbol{k}_\perp = (k_x, k_y, 0)$ perpendicular to the c axis. The interaction integral $\gamma_0 = 3.03\,\mathrm{eV}$ and overlap integral $s = 0.13$ have been obtained by fitting Eq. (4.1) to ab-initio calculations [Sai98].

The resulting graphene band structure is plotted in Fig. 4.3 where valence and conduction band exhibit the typical conical shape near the only contact points K and K′, that is

$$\left.\begin{matrix}\epsilon_{\boldsymbol{k}\pi^*}\\ \epsilon_{\boldsymbol{k}\pi}\end{matrix}\right\} \approx \pm\frac{\sqrt{3}}{2} a_0 \gamma_0 \left|\boldsymbol{k}_\perp - \overrightarrow{\Gamma\mathrm{X}}\right| \quad \text{with} \quad \mathrm{X} \in \{\mathrm{K}, \mathrm{K}'\}. \tag{4.2}$$

As a consequence, the π band is completely filled in the ground state whereas the π^* band is empty. Thus, the Fermi energy is $\epsilon_\mathrm{F} = 0$, and the Fermi surface merely consists of the HKH and H′K′H′ edges of the graphite Brillouin zone in Fig. 4.3(a). The vanishing eDOS at ϵ_F makes graphene a zero-gap semiconductor.

The graphene model provides a qualitative understanding of various properties of graphite, for example the rough location of the Fermi surface and the optical properties in the visible [Ped03]. It can also qualitatively explain the experimental data of this chapter. Moreover, a graphene sheet is a good starting point for modeling the electronic structure of carbon nanotubes (see Section 5.3). However, quantitative statements, especially about the electromagnetic response in the THz range, require a more detailed knowledge of the

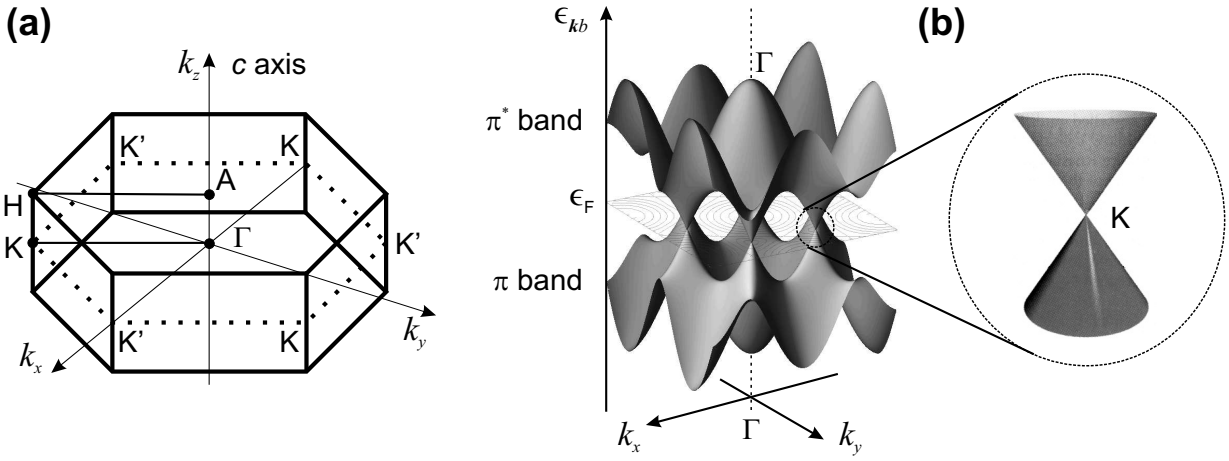

Figure 4.3.: (a) Conventional hexagonal BZ of graphite. (b) Band structure of graphene. Due to the neglected coupling between the graphene sheets, the bands depend only on k_x and k_y. The π band is completely filled in the ground state and touches the empty π^* band at the K and K′ points where both bands have conical shape. The Fermi surface consists of the HKH and H′K′H′ edges in panel (a). Parts of this figure were taken from [Hag05a].

low-energy electronic states which is provided by the model of Slonczewski, Weiss, and McClure (SWM).

4.3.2. Slonczewski-Weiss-McClure Model

In the graphene model of graphite, the π bands are degenerate with respect to k_z, whereas for fixed k_z, a 2-fold degeneracy (without counting spin) remains which stems from the equivalence of non-interacting A and B graphene layers. Taking into account the layer-layer interaction lifts these degeneracies and splits the energy bands by up to 1 eV.

The SWM model is a semi-phenomenological band model of graphite and results in a 4×4 Hamiltonian that is compatible with the symmetries of the graphite lattice [Dre88]. It involves 7 free parameters which can be determined by fits to results of appropriate experiments or ab-initio calculations. The SWM model exploits that the Fermi surface of graphite lies in the proximity of the HKH and H′K′H′ line in the BZ as suggested by the graphene model in Fig. 4.3. Here, we choose the alternative BZ shown in Fig. 4.6(a) which puts the Fermi surface in the zone center. Thus, the electron wavevectors of interest are

$$\boldsymbol{k} = \boldsymbol{k}_c + \boldsymbol{k}_\perp = \boldsymbol{k}_c + \overrightarrow{\Gamma \mathrm{X}} + \boldsymbol{\kappa} \quad \text{with} \quad \mathrm{X} \in \{\mathrm{K}, \mathrm{K}'\},$$

where $\boldsymbol{k}_c = (0, 0, k_c)$ and $\boldsymbol{k}_\perp$ are the $\boldsymbol{k}$ components parallel and perpendicular to the c axis, respectively. The small translation $\boldsymbol{\kappa}$ is expressed in cylindrical coordinates as

$$\boldsymbol{\kappa} = \kappa \begin{pmatrix} \cos\alpha \\ \sin\alpha \\ 0 \end{pmatrix}$$

where α is the angle between $\boldsymbol{\kappa}$ and $\overrightarrow{\Gamma\mathrm{K}}$.

In the 1st step, the Bloch states $|k\rangle = |\boldsymbol{k}b\rangle$ for all points $\boldsymbol{k}_c + \overrightarrow{\Gamma\mathrm{X}}$ on the high-symmetry lines HKH and H′K′H′ are determined by a tight-binding approach since the p_z overlap of adjacent layers is small; this yields 4 states for each point. In the 2nd step, the $\boldsymbol{k}\cdot\hat{\boldsymbol{\pi}}$ method is applied to wavevectors slightly off the high-symmetry lines by rewriting the stationary Schrödinger equation $\hat{H}|k\rangle = \epsilon_k|k\rangle$ for the Bloch factors u_k as [Pri91]

$$\hat{H}_{\boldsymbol{k}}u_k = \epsilon_k u_k \quad \text{with} \quad \hat{H}_{\boldsymbol{k}} = \frac{(\hat{\boldsymbol{\pi}} + \hbar\boldsymbol{k})^2}{2m_\mathrm{e}} + \text{single-electron potential.}$$

By neglecting quadratic effects in $\boldsymbol{\kappa}$, the Hamiltonian becomes

$$\hat{H}_{\boldsymbol{k}} = \hat{H}_{\boldsymbol{k}_c+\overrightarrow{\Gamma\mathrm{X}}} + \frac{\hbar}{m_\mathrm{e}}\boldsymbol{\kappa}\hat{\boldsymbol{\pi}}. \tag{4.3}$$

In the basis of the tight-binding states $|\boldsymbol{k}_c + \overrightarrow{\Gamma\mathrm{X}}, 1\rangle, \ldots, |\boldsymbol{k}_c + \overrightarrow{\Gamma\mathrm{X}}, 4\rangle$, this finally gives the SWMcC Hamiltonian

$$H_{\boldsymbol{k}} = \begin{pmatrix} E_1 & & & \\ & E_2 & & \\ & & E_3 & \\ & & & E_3 \end{pmatrix} + \sigma \begin{pmatrix} 0 & & h_{13} & h_{13}^* \\ & 0 & h_{23} & -h_{23}^* \\ h_{13}^* & h_{23}^* & 0 & h_{33} \\ h_{13} & -h_{23} & h_{33}^* & 0 \end{pmatrix}. \tag{4.4}$$

Its diagonalization leads to 4 states and 4 eigenenergies for each $\boldsymbol{k}$ in the vicinity of the HKH or H′K′H′ line; the eigenenergies for points lying exactly on this line ($\sigma = 0$) are

$$\left.\begin{matrix} E_1 \\ E_2 \end{matrix}\right\} = \Delta \pm \gamma_1\Gamma \quad \text{and} \quad E_3 = \frac{1}{2}\gamma_2\Gamma^2$$

where the dimensionless parameters

$$\xi = \frac{k_z c_0}{2\pi}, \quad \Gamma = 2\cos(\pi\xi), \quad \text{and} \quad \sigma = \frac{\sqrt{3}}{2}a_0\kappa$$

have been introduced. The off-diagonal elements of the Hamiltonian are given by

$$\left.\begin{matrix} h_{13} \\ h_{23} \end{matrix}\right\} = (\mp\gamma_0 + \gamma_4\Gamma)\frac{\exp(\mathrm{i}\alpha)}{\sqrt{2}} \quad \text{and} \quad h_{33} = \gamma_3\Gamma\exp(\mathrm{i}\alpha)$$

where the 7 phenomenological parameters $\gamma_0, \ldots, \gamma_5$, and Δ can be estimated by tight-binding calculations which also elucidate their physical meaning. However, they have been determined by fits to various experimental results.

Like in graphene, $\gamma_0 = 3.16\,\mathrm{eV}$ is the interaction integral of adjacent C atoms from the *same* layer; the interaction integral $\gamma_1 = 0.39\,\mathrm{eV}$ of 2 adjacent C atoms from *different* layers is mainly responsible for the splitting of the originally multi-degenerate bands. These and all other values of the phenomenological parameters together with their interpretation can be

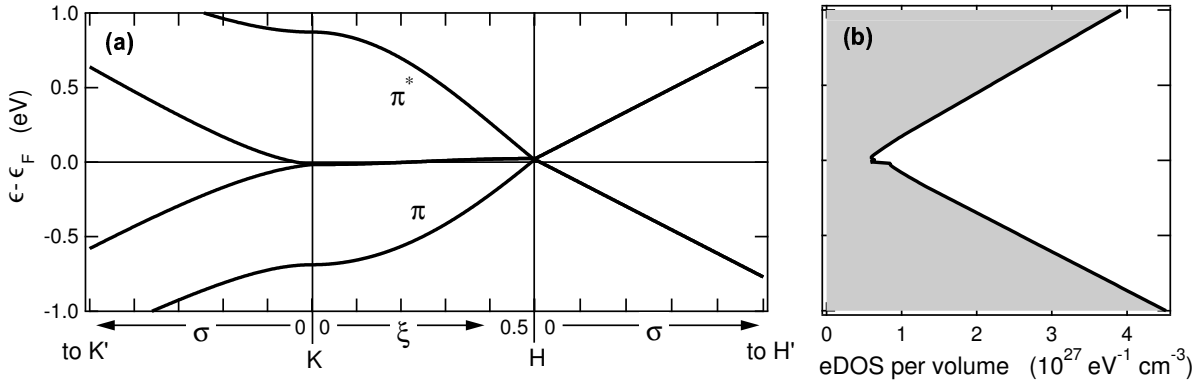

Figure 4.4.: (a) Band structure of graphite close to the HKH high symmetry line calculated according to Eq. (4.4). Note that, like for graphene, the Fermi surface lies around the HKH line. The dependence on the polar angle α is weak close to the Fermi edge but leads to a trigonal warping of the bands at energies $|\epsilon - \epsilon_\mathrm{F}| > 1\,\mathrm{eV}$ [Dre88]. (b) Resulting electronic density of states.

found in Ref. [Dre88]. They also fix the Fermi energy at $\epsilon_\mathrm{F} = -0.024\,\mathrm{eV}$. Importantly, the momentum matrix elements projected on the $\boldsymbol{\kappa}$ direction can be obtained by comparing Eqs. (4.3) and (4.4). They are essential for the calculation of the optical properties. As an illustration of the SWM model, Fig. 4.4 shows the band structure of graphite close to the HKH line and the resulting eDOS whose smallness at the Fermi energy makes graphite a semimetal. Computational details are described in Appendix C.1.

In summary, the semiphenomenological Hamiltonian (4.4) was developed by SWM to obtain the band structure and momentum matrix elements in the vicinity of the Fermi energy ϵ_F with 7 free parameters which have been determined by experimental data [Dre88]. It will be used extensively in the following to model the measured dielectric function of graphite between 1 and 30 THz.

4.4. Phonons and Their Coupling to Electrons

The strong sp^2-bonds and the low mass of the C atom lead to lattice vibrations of very high frequency as can be seen in Fig. 4.5 where phonon energies $\hbar\Omega_Q$ of up to 0.2 eV are found.

In general, electrons can partially screen the bare ion-ion interaction and thus soften the lattice vibrations in a solid. Such screening of a vibrational mode $Q = (r, \boldsymbol{q})$ requires virtual electronic transitions which have to conserve the electronic wavevector $\boldsymbol{k}$ [Pis04, Ash76]. In graphite, the Fermi surface restricts the component $\Delta\boldsymbol{k}_\perp$ of the change $\Delta\boldsymbol{k} = \Delta\boldsymbol{k}_c + \Delta\boldsymbol{k}_\perp$ in the electronic wavevector to the vicinity of the Γ and K points, that is

$$\Delta\boldsymbol{k}_\perp \approx \overrightarrow{\mathrm{KK}} = 0 \quad \text{or} \quad \Delta\boldsymbol{k}_\perp \approx \overrightarrow{\mathrm{KK}'} = \overrightarrow{\Gamma\mathrm{K}}.$$

Figure 4.6 illustrates these intrapocket and interpocket transitions of the electrons. Therefore, only phonons with $\boldsymbol{q}_\perp$ around Γ or K and strong coupling to the electrons can suffer

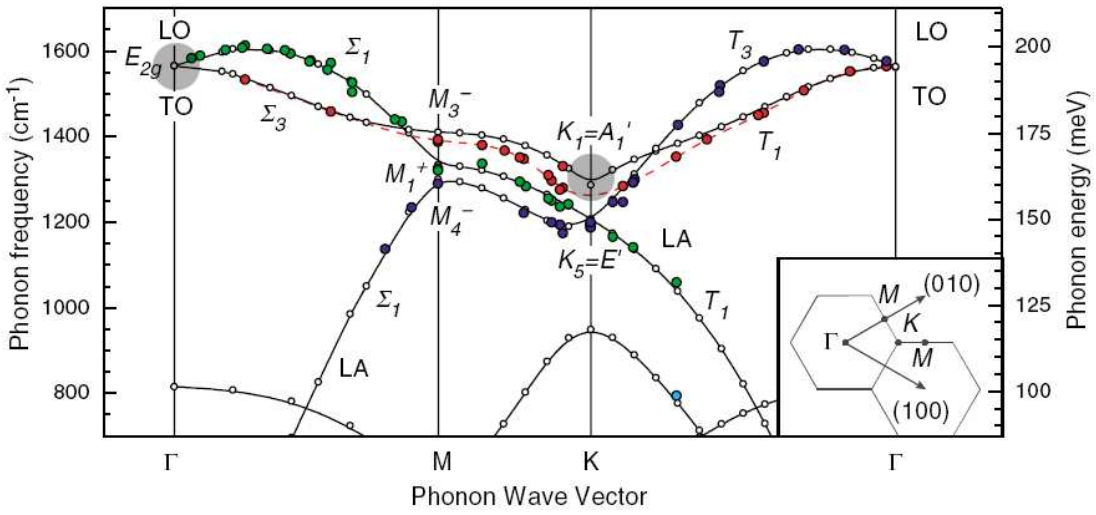

Figure 4.5.: Dispersion curves $\hbar\Omega_Q$ of the high-energy phonons in graphite taken from Ref. [Mau04]. Symbols (○ and ●) represent data taken by inelastic X-ray scattering whereas solid lines are fits to a force-constant calculation. The shaded areas at the Γ and K point are Kohn anomalies caused by the strong e-ph coupling of these phonon modes.

softening. This is nicely seen in Fig. 4.5 where the Γ and K phonons of the highest energy exhibit kinks in their dispersion curves. These so-called Kohn anomalies are absent for all other modes with lower phonon energy since their e-ph matrix elements vanish as shown by density-functional theory calculations for *graphene* [Pis04]. In *graphite*, however, there should be some coupling to these modes due to dispersion along $\boldsymbol{k}_c$ [Ash76].

4.5. Optical Properties

No infrared-active phonon modes have been observed in graphite in the far- and mid-infrared [Pal91]. The main reason for this behavior is a very small static dipole moment of the nonpolar graphite lattice in contrast to ionic crystals like NaCl [Kim05]. This situation corresponds to a Lorentz oscillator where the particle interacting with the light has a very small charge, see Section 1.5.1.

The optical properties in the infrared and visible spectrum are dominated by electronic transitions. As explained in Section 1.6 and shown in Fig. 4.7, a Bloch electron can either absorb a photon by a *direct* optical transition (DOT) or by an *indirect* optical transition (IOT). As will be shown below, IOTs dominate the optical absorption in the far-infrared; both IOTs and DOTs are important in the mid-infrared, and DOTs dominate in the near-infrared and visible.

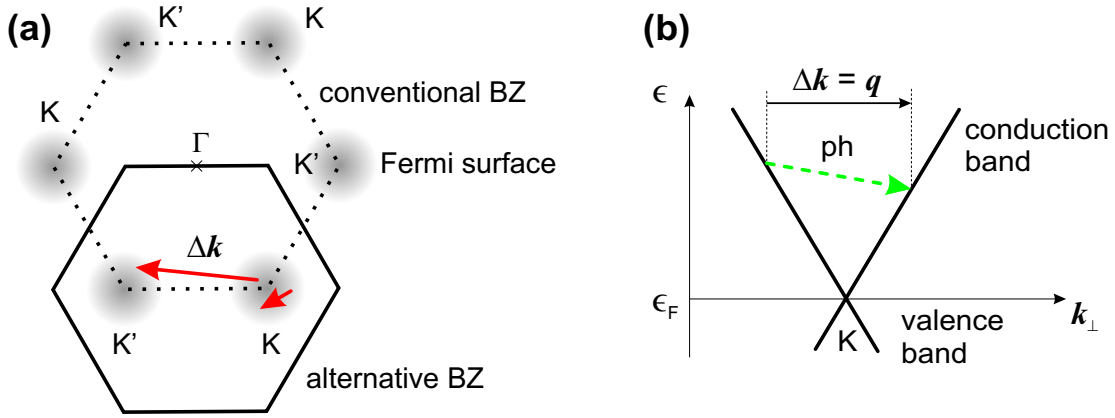

Figure 4.6.: (a) Cross section of the BZ at $k_z = 0$ together with a pictorial view of the Fermi surface and an intrapocket and interpocket electron transition. Intrapocket scattering does nearly not change the electron wavevector $\boldsymbol{k}_\perp$ perpendicular to the c axis whereas interpocket scattering requires a wavevector change $\Delta\boldsymbol{k}_\perp$ in proximity to the K point. (b) Graphene band structure around the K point together with an intrapocket scattering event by phonon emission.

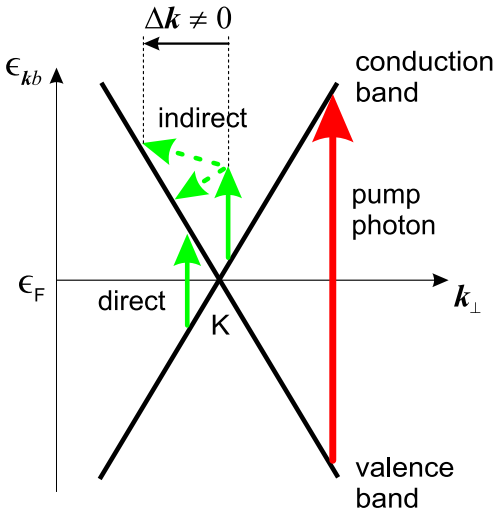

Figure 4.7.: Graphene band structure close to the K point. Arrows indicate possible direct and indirect optical transitions induced by the THz probe pulse and a direct optical transition triggered by the visible pump pulse. An indirect transition involves a change $\Delta\boldsymbol{k}$ of the electron wavevector. In graphite and graphene, $\Delta\boldsymbol{k}_\perp$ is restricted to the vicinity of the Γ and K point.

4.6. Experimental and Technical Details

4.6.1. Sample Preparation

The sample base material is a high-purity crystal of HOPG (quality ZYB, GE Advanced Ceramics) with a thickness of 2 mm along the c axis and a 12×12-mm^2 front surface area. The crystal is cleaved perpendicular to the c axis by means of sticky tape (tesa kristallklar, Beiersdorf AG) which is fixed to the crystal front surface. After careful removal from the crystal, graphite flakes are attached to the tape and used for the measurements. The area probed in the experiment is selected by transmission measurements at a wavelength of 780 nm in which the sample is put in the focus of the THz beam but with the Si filter removed. By using the formalism of Section 2.5.1, the local thickness of the graphite

film with a transverse spatial resolution better than 30 μm is determined. We exclusively choose graphite areas which show transmission changes less than 10 % on an area larger than $0.2 \times 0.2\,\mathrm{mm}^2$.

For the pump-probe measurements, the sample is contacted to a diamond substrate, as sketched in Fig. 4.8(a). Otherwise, the thermal load of the sticky tape and the graphite would destroy the sample.

4.6.2. Sample Pumping and Probing

In all measurements, the THz beam is normally incident on the sample and thus probes the optical properties parallel to the graphite layers. In general, the graphite film should be as thick as possible to obtain phase shifts much larger than the phase drift of the spectrometer as discussed in Section 3.2.4. On the other hand, the sample thickness is limited since graphite absorbs light strongly.

The 53-nm thick sample taken for the steady-state measurements is a good compromise. They were done without the diamond substrate which would introduce significant phase shifts between sample and reference signal owing to its thickness variations. We checked that the thickness variations of the sticky tape are negligible making this material a good reference sample.

In the pump-probe measurements, the pump beam is aligned such that pump and probe spot overlap on the sample. The angle between the pump and probe direction of propagation is smaller than 10° to excite all points of the probed sample spot within less than 40 fs. Using a graphite film thicker than the 33-nm penetration depth of the pump beam generates an inhomogeneous excitation profile

$$P_\tau(z) = \frac{\Delta\varepsilon_\tau(z)}{\Delta\varepsilon_\tau(0)} \tag{4.5}$$

which will rapidly change its shape due to transport processes, until a homogeneous profile $P_\tau = 1$ is established. This effect may complicate the extraction of the dielectric function from the data but can be circumvented by ensuring a homogeneous excitation profile immediately after sample excitation. For this purpose, we use a graphite film of only 17 nm thickness which results in $P_{\tau=0^+} \approx 1$ directly after excitation as shown in Fig. 4.8(b). The profile was calculated using the relation

$$\Delta\varepsilon_{\tau=0^+}(z) \propto |E(\omega_{\mathrm{pump}}, z)|^2$$

which is valid for a 1-photon excitation process and small pump-induced changes $\Delta\varepsilon_\tau(z)$ [Jas02]. The electric field $E(\omega_{\mathrm{pump}}, z)$ of the pump beam is given by Eq. (2.12) with $\hbar\omega_{\mathrm{pump}} = 1.6\,\mathrm{eV}$.

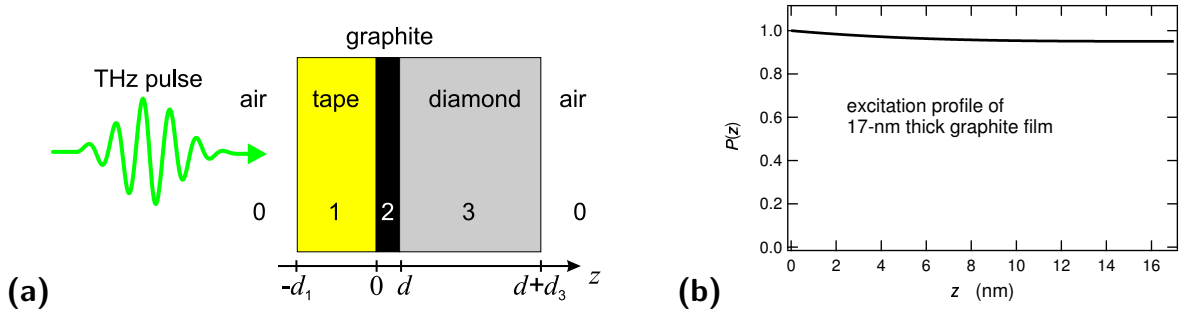

Figure 4.8.: (a) Schematic of the graphite sample. The graphite film (2) is fixed to a diamond substrate (3) by sticky tape (1). The THz wave is normally incident on the sample and propagates along the z axis which is parallel to the graphite c axis. In the steady-state measurements, the diamond substrate is not used. (b) Calculated excitation profile for the sample in (a) with a 17-nm thick graphite film.

4.6.3. Data Analysis

As described in general in Section 3.4, the dielectric function of the unexcited and excited sample can be determined from the respective experimental data

$$Q(\omega) = \frac{S(\omega)}{S_{\mathrm{ref}}(\omega)} \quad \text{and} \quad \Delta Q_\tau(\omega) = \frac{\Delta S_\tau(\omega)}{S_\infty(\omega)}.$$

Here, S is the THz signal of the sample in the steady state and S_{ref} the reference signal without graphite; ΔS_τ is the pump-induced signal at a delay τ after excitation, and S_∞ the signal of the sample long after or before the arrival of the pump pulse.

Unexcited Sample

Figure 4.8(a) shows the structure of the sample. Although the beam propagates through the 3 layers 1, 2, and 3, "echoes" due to multiple reflections in the tape (1) and the diamond substrate (3) are outside the temporal window covered in the THz detection. Therefore, the sample can be seen as a film between 2 homogeneous half spaces, and Eq. (2.12) yields the response

$$R = \frac{E(d + d_3 + 0^+, \omega)}{E_{\mathrm{inc}}(\omega)} = t_{01} \exp(\mathrm{i}k_1 d_1) \cdot A_3^+ \cdot \exp(\mathrm{i}k_3 d_3) t_{30}$$

of the 3-layer system in Fig. 4.8(a) where the 1st and the last factor account for a single transmission through layer 1 and 3, respectively. All quantities in this equation are defined in Section 2.5.1.

The response of the reference sample fulfills the same relation but with the transmission through graphite replaced by a single transmission through air (0), that is

$$R_{\mathrm{ref}} = \frac{E_{\mathrm{ref}}(d + d_3 + 0^+, \omega)}{E_{\mathrm{inc}}(\omega)} = t_{01} \exp(\mathrm{i}k_1 d_1) \cdot \exp(\mathrm{i}k_3 d_3) t_{30} \cdot \exp(\mathrm{i}k_0 d).$$

Division of the last 2 equations finally yields

$$Q\exp(\mathrm{i}k_0 d) = A_3^+ = \frac{t_{12}t_{23}}{\exp(-\mathrm{i}\delta) - r_{21}r_{23}\exp(\mathrm{i}\delta)} \tag{4.6}$$

with $\delta = kd$ being the phase shift of the graphite film. Note that a perfect cancelation of the phase factors only occurs when the thickness of tape and substrate is the same for both the sample and the reference measurement. For this reason, the steady-state measurements are done *without* diamond substrate, $n_3 = n_0 = 1$.

Equation (4.6) contains the desired $\varepsilon = n^2$ in the exp, t_{ij}, and r_{ij} terms and can in general be solved only numerically. However, in case of a thin layer 2, that is $\delta = kd = \omega nd/c \ll 2\pi$, one can expand $\exp(\mathrm{i}\delta) \approx 1 + \mathrm{i}\delta - \delta^2/2$ up to 2nd order to obtain [Sch05]

$$A_3^+ = Q\exp(\mathrm{i}k_0 d) = \frac{2n_1}{(1-\delta^2/2)(n_1+n_3) - \mathrm{i}(n^2 + n_1 n_3)\delta/n}$$

which now allows to analytically solve for

$$\varepsilon = -\frac{c}{\omega d}\frac{2n_1\exp(-\mathrm{i}k_0 d)/Q + \mathrm{i}n_1 n_3 \omega d/c - n_1 - n_3}{\mathrm{i} + (n_1+n_3)\omega d/2c}. \tag{4.7}$$

This "thin-film formula" is correct to the 2nd order in δ and is an improvement of the 1st-order formula used in the literature [Ave02].

We use $n_1 = 1.46$ for the sticky tape as obtained by THz transmission measurements covering the spectral range from 1 to 3 THz and 10 to 30 THz whereas $n_3 = 2.38$ for diamond is taken from literature [Pal91].

Excited Sample

We do not observe a pump-induced optical anisotropy perpendicular to the graphite c axis since the signal does not change for different pump-beam polarizations (data not shown). Therefore, the response in this plane is determined by only 1 scalar dielectric function. Since the graphite film is much thinner than the probing wavelength we can apply Eq. (2.16), and the pump-induced change in the sample response is

$$\Delta R_\Omega(\omega - \Omega) = \frac{\Delta E_\tau(d+0^+,\omega)}{E_{\mathrm{inc}}(\omega-\Omega)} = \frac{\mathrm{i}\omega}{2cn_1(\omega)} R_\infty(\omega) R_\infty(\omega-\Omega)\, d\Delta\varepsilon_\Omega(\omega-\Omega).$$

Here we have exploited that the graphite sample is homogeneously excited, and the response R_∞ of the unexcited sample is approximated by Eq. (2.14). According to Eq. (3.1), $\Delta R_\Omega(\omega-\Omega) \approx R_\infty(\omega)\Delta Q_\Omega(\omega)$ which finally yields the pump-induced change

$$\Delta\varepsilon_\Omega(\omega) = \frac{2cn_1(\omega+\Omega)}{\mathrm{i}\cdot(\omega+\Omega)dR_\infty(\omega)}\Delta Q_\Omega(\omega+\Omega). \tag{4.8}$$

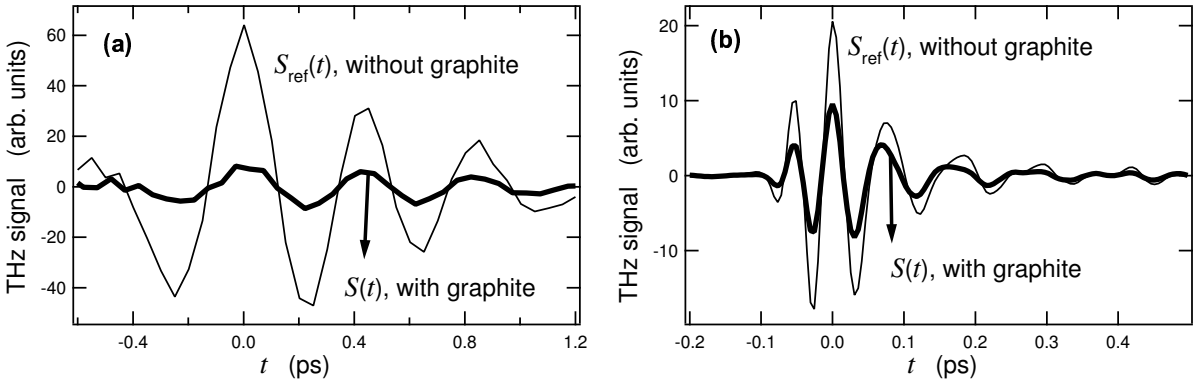

Figure 4.9.: (a) THz signals S and S_{ref} after transmission through a sample containing a 53-nm thick graphite film and a sample without graphite, respectively. The probe pulse covers the spectrum from 1 to 3 THz and experiences a significant amplitude decrease but only a small phase shift upon transmission through the graphite. (b) Same as (a), but for an 8-to-30-THz pulse.

By applying an inverse Fourier transformation with respect to Ω, one obtains the the pump-induced change $\Delta\varepsilon_\tau(\omega)$ in the dielectric function at time τ after sample excitation. If the sample does not change too fast, one can set $\omega + \Omega \approx \omega$ leading to the quasistatic result

$$\Delta\varepsilon_\tau(\omega) = \frac{2cn_1(\omega)}{\mathrm{i}\omega d R_\infty(\omega)} \Delta Q_\tau(\omega).$$

We found this relation to give results in good agreement with the more general Eq. (4.8) for $\tau > 0.1\,\mathrm{ps}$.

4.7. Results: Unexcited Sample

The following measurements of the sample in the steady state provide the parameters necessary to analyze the pump-probe measurements. The raw data of a steady-state measurement is shown in Fig. 4.9. Note that the graphite film introduces a very small phase shift but a significant amplitude decrease of the THz signal. The dielectric function is calculated according to Eq. (4.7); we start with a discussion of the 1-to-3-THz range.

4.7.1. Dielectric Function Between 1 and 3 THz

The dielectric function ε of graphite between 1 and 3 THz is shown in Fig. 4.10. Note that $\mathrm{Re}\,\Delta\varepsilon$ is negative and increases with decreasing frequency. According to Section 1.6.1, this is a clear signature of free charge carriers. Indeed, intraDOTs and IOTs are expected to dominate the response in this frequency window since the SWM model together with Eq. (1.19) predicts negligible contributions of interDOTs as can be seen in Fig. 4.10. Technical details concerning this calculation are found in Appendix C.1.

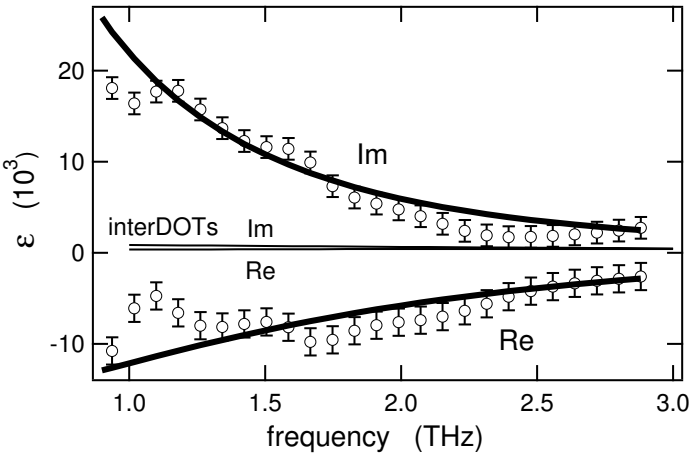

Figure 4.10.: Measured dielectric function of graphite (○) between 1 and 3 THz together with a fit to the Drude model (thick solid line). The Drude contribution is expected to dominate the response since the theoretical contribution of interDOTs (thin solid line) is much smaller than the measured ε. The dielectric function is the average of measurements on 3 different sample positions, and the error bars represent the resulting standard deviation.

We fit the dielectric function to the Drude formula (1.12) where the fit parameters are the plasma frequency Ω_{pl} and the Drude scattering rate Γ. The best fit is shown in Fig. 4.10 and obtained for the values

$$\hbar\Omega_{\mathrm{pl}} = 0.92\,\mathrm{eV} \text{ and } \Gamma = 10\,\mathrm{THz}. \tag{4.9}$$

The agreement with the values $\hbar\Omega_{\mathrm{pl}} = 0.44\,\mathrm{eV}$ and $\Gamma = 5\,\mathrm{THz}$ found in Ref. [Phi77] is reasonable if one takes into account that they have been obtained by Fourier-transform infrared spectroscopy on naturally grown graphite and by subsequent application of the Kramers-Kronig relations.

Moreover, the measured plasma frequency of graphite agrees excellently with the theoretical value of 1.0 eV calculated here using Eq. (1.22), the SWM model, and an electronic temperature of 300 K. The plasma frequency is small compared to that of normal metals like Al with $\hbar\Omega_{\mathrm{pl}} = 9.2\,\mathrm{eV}$ [Ash76] which is just a result of the small eDOS around the Fermi edge of the semimetal graphite.

The measured Γ and the band velocity (1.20) of $\approx 1\,\mathrm{nm\,fs^{-1}}$ at the Fermi edge [Dre88] imply a mean free path of $\approx 100\,\mathrm{nm}$ for the electrons moving parallel to the graphite layers. In other words, they pass more than 300 unit cells before collisions with obstacles have completely randomized their initial velocity. In contrast, the Fermi velocity of $2\,\mathrm{nm\,fs^{-1}}$ and the scattering rate of 125 THz in Al lead to a mean free path of only 20 nm [Ash76]. The reason for this behavior is again mainly the small density of states at the Fermi energy which restricts the number of possible electronic scattering events, see also Eq. (1.27).

4.7.2. Dielectric Function Between 8 and 27 THz

The dielectric function of graphite between 8 and 27 THz is shown in Fig. 4.11(a). It cannot be explained by the extrapolated Drude behavior found for the dielectric function between 1 and 3 THz since the imaginary part of the Drude tail remains way below that measured.

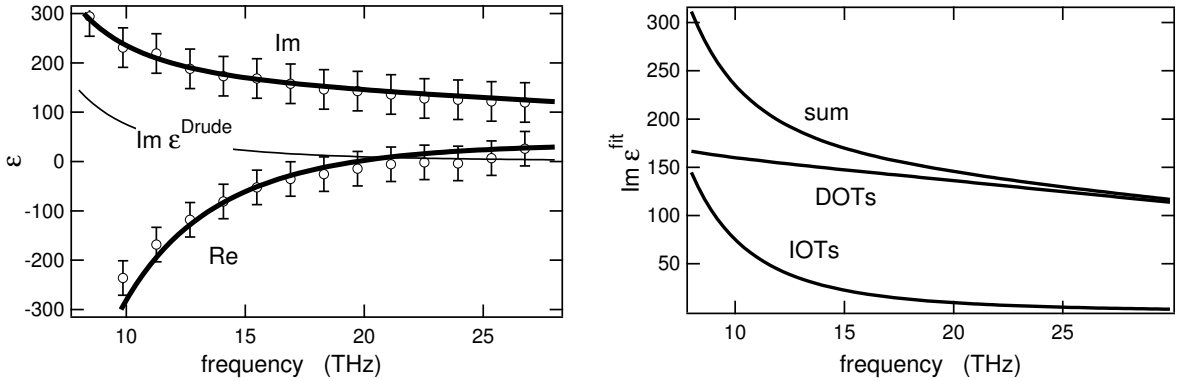

Figure 4.11.: (a) Measured dielectric function of graphite (○) between 8 and 27 THz together with the fit (thick solid line) to Eq. (4.10). The dielectric function is the average of 5 measurements at different sample positions, and the error bars represent the resulting standard deviation. (b) Contributions of DOTs and IOTs to the fit to $\mathrm{Im}\,\varepsilon$.

Therefore, now DOTs have to make a strong contribution to the light absorption, and we fit the dielectric function to

$$\varepsilon^{\mathrm{fit}} = \varepsilon^{\mathrm{Drude}} + C\varepsilon^{\mathrm{interDOT}} + \text{real offset}. \tag{4.10}$$

$\varepsilon^{\mathrm{interDOT}}$ is calculated using Eq. (1.19), the SWM band model, and an electronic temperature of $T_{\mathrm{e}} = 300\,\mathrm{K}$, for details see Appendix C.1. $\varepsilon^{\mathrm{Drude}}$ is given by the Drude formula (1.12) and Eq. (4.9). The only fit parameters are a real factor C, which scales the contribution of the DOTs, and a real offset which accounts for optical transitions with resonances outside the frequency window considered.

The best fit result is shown in Fig. 4.11(a) and obtained for $C = 0.65$ and a real offset of 38. Figure 4.11(b) shows the respective contributions of IOTs and DOTs to $\mathrm{Im}\,\varepsilon$. For $C = 1$ and above 20 THz, the imaginary part of the fit function would be significantly larger than the experimental result. This behavior is most likely due to local-field effects which are neglected in the theory of the dielectric function as mentioned in Section 1.5.4. They are roughly accounted for by the overall scaling factor $C < 1$.

In summary, DOTs and IOTs make comparable contributions to the absorption of electromagnetic radiation between 8 and 27 THz in graphite. This behavior is exploited for the time-resolved measurements where the DOTs serve as a "thermometer" of the electrons and the IOTs as a probe for the velocity relaxation of the electrons. In contrast, the absorption of visible probe pulses in graphite is mediated mainly by DOTs. They have been exploited to determine the distribution function of the electrons at very high fluences by time-resolved transmission and reflection measurements [Sei90].

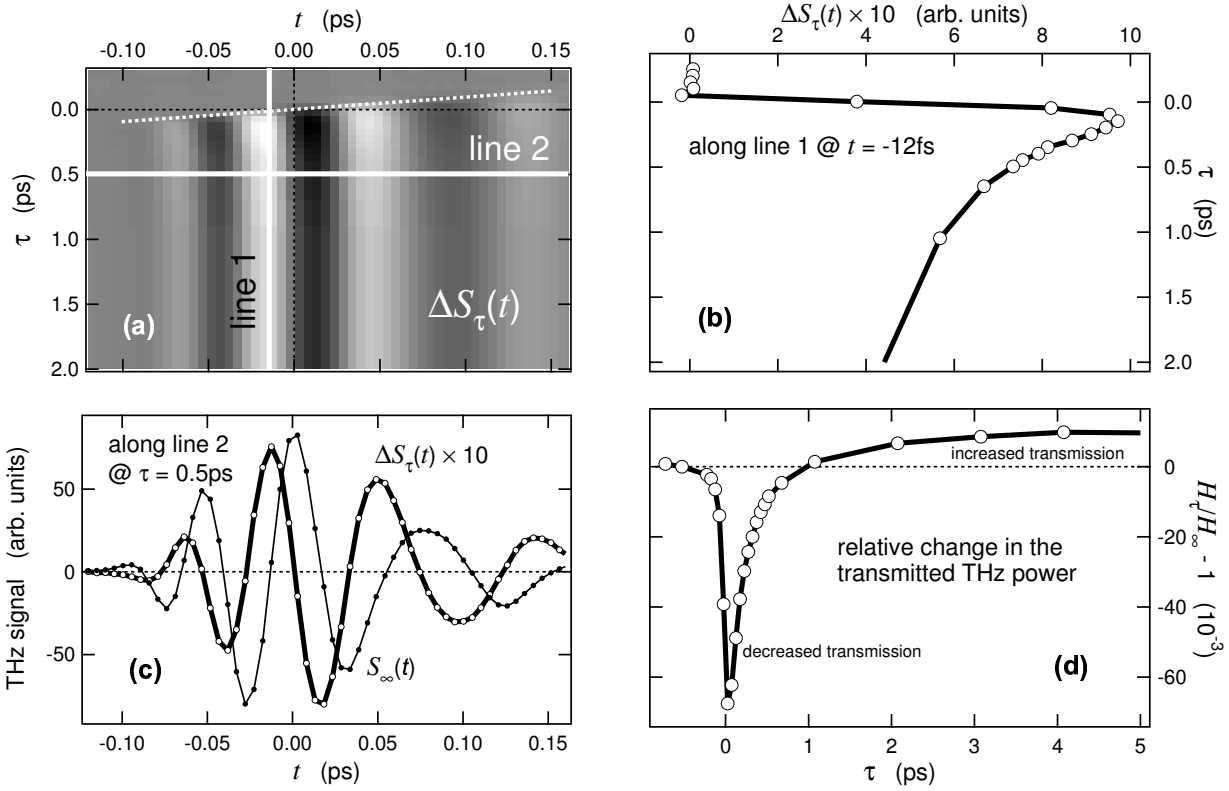

Figure 4.12.: Raw data of the TRTS measurements of graphite for an absorbed fluence of $5\,\mu\mathrm{J\,cm^{-2}}$. (a) Gray-scale plot of the 2-dimensional pump-induced THz signal $\Delta S_\tau(t)$. There is no signal for larger negative pump-probe delays τ where the pump pulse arrives at the sample long after the probe pulse. At $\tau = 0$, the center of pump and probe pulse arrive simultaneously at the sample, and the trailing part of the probe pulse ($t > 0$) already sees an excited sample whereas the leading part ($t < 0$) still does not. This behavior is marked by the white dashed diagonal line. (b) Line scan along line 1 where the local THz time is fixed at $t = -12\,\mathrm{fs}$. (c) Line scan along line 2 for a constant pump-probe delay $\tau = 0.5\,\mathrm{ps}$. The signal $S_\infty(t)$ of the unperturbed sample is also shown and exhibits a phase shift of $\approx 90°$ with respect to $\Delta S_\tau(t)$. (d) Relative change $H_\tau/H_\infty - 1$ in the power of the transmitted THz pulse according to Eq. (4.11). There is a crossover from decreased to increased transmission at $\tau \approx 1\,\mathrm{ps}$.

4.8. Results: Excited sample

4.8.1. Raw Data

Figure 4.12 shows the raw data $\Delta S_\tau(t)$ of a TRTS experiment where the graphite film absorbs a pump fluence of $5\,\mu\mathrm{J\,cm^{-2}}$ corresponding to a molar energy density of $W_{\mathrm{pump}} = 18\,\mathrm{J\,mol^{-1}}$. The dashed diagonal line $t + \tau = 0$ in the 2-dimensional gray-scale plot of $\Delta S_\tau(t)$ in Fig. 4.12(a) defines the times when the pump pulse and the overlapping portion of the probe pulse arrive simultaneously at the sample.

A line scan along the vertical line $t = -12\,\mathrm{fs}$ is plotted in Fig. 4.12(b) and exhibits a fast signal rise and a decay on a ps time scale. The line scan along the horizontal line $\tau = 0.5\,\mathrm{ps}$

is plotted in Fig. 4.12(c). The phase shift between ΔS_τ and S_∞ is $\approx 90°$ indicating that the pump-induced sample response is dominated by dispersion, that is by $\mathrm{Re}\,\Delta\varepsilon_\tau$. In this case, the excited sample induces phase shifts of the THz wave rather than amplitude decreases which are due mainly to $\mathrm{Im}\,\Delta\varepsilon_\tau$.

Since the THz signal is roughly proportional to the electric field at the detector, the energy per THz pulse transmitted through the sample is roughly proportional to

$$H_\tau = \int \mathrm{d}t\, S_\tau(t)^2. \tag{4.11}$$

Therefore, $H_\tau/H_\infty - 1$ is approximately the pump-induced change in the THz power transmitted through the sample. It is plotted in Fig. 4.12(d) and reveals that the sample transmission decreases directly after excitation and later turns into an increased transmission. A spectral analysis is absolutely necessary to disentangle the processes causing this response.

4.8.2. Dynamics of the Dielectric Function and Model Fits

Dynamics of the Dielectric Function

The pump-induced changes $\Delta\varepsilon_\tau(\omega)$ in the dielectric function are calculated according to Eq. (4.8), and the results are plotted for 3 exemplary delays and for frequencies $\omega/2\pi$ between 10 and 26 THz in Fig. 4.13.

As already expected from the raw data, the real part dominates the optical response. Moreover, it is negative and decreasing towards higher frequencies which is the typical signature of a free-carrier response as detailed in Section 1.6.

The imaginary part of all spectra shows 2 remarkable features: For the lower frequencies, we find $\mathrm{Im}\,\Delta\varepsilon_\tau > 0$ and thus increased absorption, whereas for the higher probe frequencies one has $\mathrm{Im}\,\Delta\varepsilon_\tau < 0$ and thus decreased absorption. This behavior can be explained by the different response of DOTs and IOTs to a change in the electronic occupation numbers as depicted in the graphene band structure of Fig. 4.7: Exciting the sample with a visible pump pulse via a DOT transfers electrons from the valence band to the conduction band. After $\approx 0.5\,\mathrm{ps}$ these hot electrons have thermalized and can be described by a Fermi-Dirac distribution with electronic temperature T_e as has been revealed by time-resolved photoemission spectroscopy (TRPES) [Moo01]. The newly created electron-hole pairs block some of the originally possible DOTs in a range of $k_\mathrm{B}T_\mathrm{e}$ around the Fermi energy ϵ_F and *decrease* the absorption of photons $\hbar\omega \sim k_\mathrm{B}T_\mathrm{e}$. However, the elevated electronic temperature enables additional IOTs thus leading to an *increased* THz absorption predominantly at the lower frequencies as suggested by Eq. (1.24). Therefore, the frequency dependence of $\mathrm{Im}\,\Delta\varepsilon_\tau$ displayed in Fig. 4.13 reflects the interplay between DOTs and IOTs in graphite.

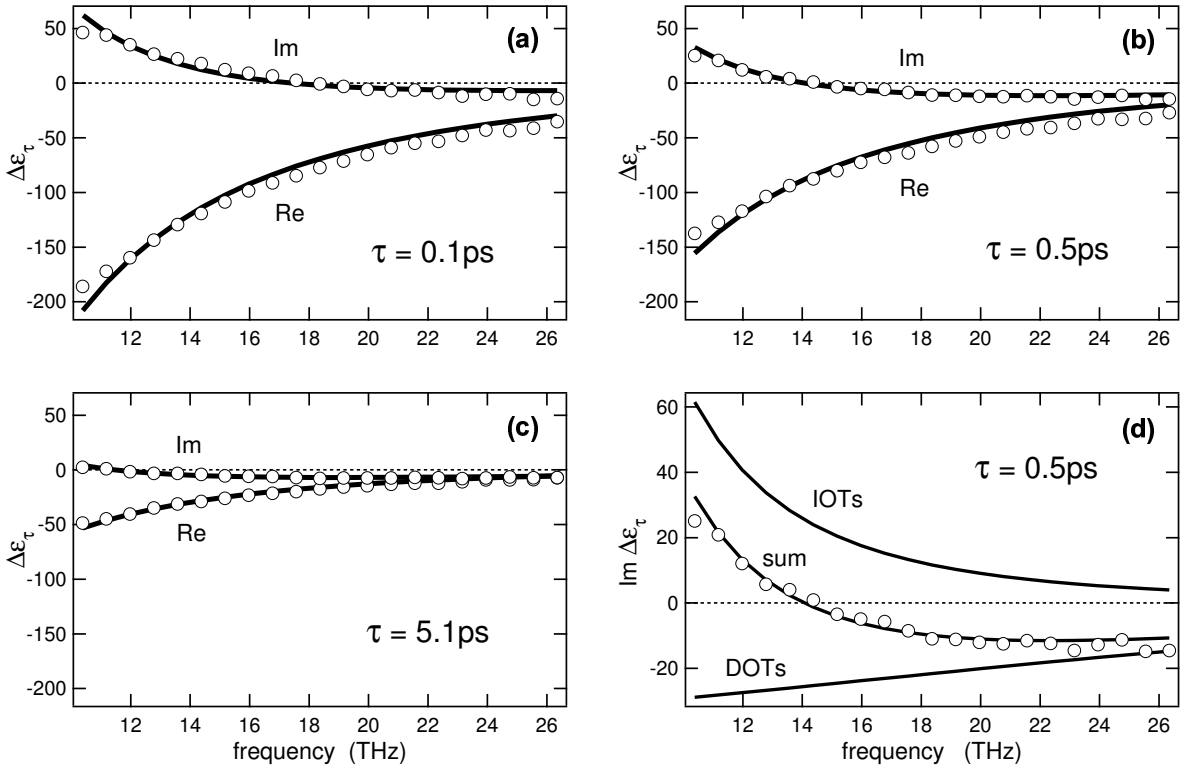

Figure 4.13.: (a,b,c) Pump-induced change $\Delta\varepsilon_\tau$ in the dielectric function of graphite (○) between 10 and 26 THz for at various times τ after excitation. Thick solid lines are fits according to Eq. (4.10). The real part exhibits a typical free-carrier response which also dominates the imaginary part at the lower frequencies. At the higher frequencies, however, the negative $\mathrm{Im}\,\Delta\varepsilon_\tau$ displays a decreased absorption induced by the blocking of DOTs. (d) Contributions of DOTs and IOTs to the fit to $\mathrm{Im}\,\Delta\varepsilon_\tau$.

Modeling of $\Delta\varepsilon_\tau$

The band structure and Bloch states of the excited graphite sample are expected to remain unchanged upon excitation by the pump pulse since the molar excitation energy of $W_{\mathrm{pump}} = 18\,\mathrm{J\,mol^{-1}}$ is quite small. For example, this corresponds to only 10^{-4} pump photons per carbon atom and an increase of the total graphite temperature T by

$$\Delta T = \frac{W_{\mathrm{pump}}}{C}. \tag{4.12}$$

This corresponds to less than 3 K according to the total heat capacity of $C \approx 9\,\mathrm{J\,mol^{-1}\,K^{-1}}$ around $T = 300\,\mathrm{K}$ [Nih03]. Moreover, we assume a thermalized electron system such that the electronic occupation numbers are given by a Fermi-Dirac distribution. The model dielectric function is the difference

$$\Delta\varepsilon_\tau^{\mathrm{fit}} = \varepsilon^{\mathrm{fit}}(T_{\mathrm{e}}, \Omega_{\mathrm{pl}}, \Gamma) - \varepsilon^{\mathrm{fit}}(T_{\mathrm{e}\infty}, \Omega_{\mathrm{pl}\infty}, \Gamma_\infty)$$

where $\varepsilon^{\mathrm{fit}}$ is the fit function (4.10) of the steady-state case. The fit parameters are now T_{e}, Ω_{pl}, and Γ. For the unexcited sample, they are fixed to $T_{\mathrm{e}\infty} = 300\,\mathrm{K}$, $\hbar\Omega_{\mathrm{pl}\infty} = 0.92\,\mathrm{eV}$,

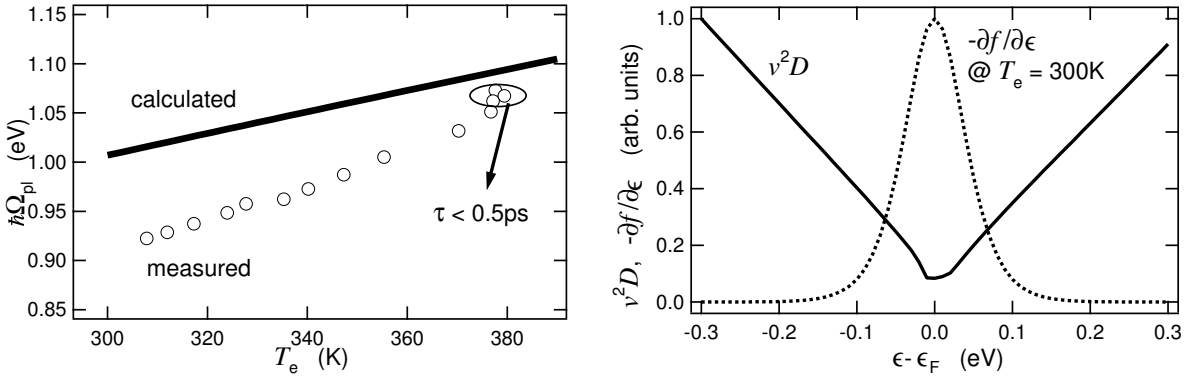

Figure 4.14.: (a) Measured transient plasma frequency $\hbar\Omega_{\mathrm{pl}}$ vs. electronic temperature T_{e} together with a theoretical calculation based on Eq. (1.22) and the SWM model. (b) Velocity-weighted density of states $v^2D(\epsilon)$ and derivative $-\partial f/\partial\epsilon$ of the Fermi-Dirac function at an electronic temperature of $T_{\mathrm{e}} = 300\,\mathrm{K}$. The width of $-\partial f/\partial\epsilon$ grows with T_{e}, and $v^2D(\epsilon)$ becomes larger beyond the Fermi energy ϵ_{F}. Therefore the squared plasma frequency Ω_{pl}^2, which is the area under the product curve $-v^2D(\epsilon)\cdot\partial f/\partial\epsilon$, increases as well.

and $\Gamma_\infty = 10\,\mathrm{THz}$. In this model, the electronic temperature completely determines the contribution of the interDOTs, whereas Ω_{pl} and Γ parametrize the contributions of the remaining, Drude-like transitions.

As shown in Fig. 4.13, the fits excellently reproduce the experimental data. The temporal dynamics of the 3 fit parameters T_{e}, Ω_{pl}, and Γ are the main outcome of the preceding analysis and basis of the following discussions. For example, the decay of the electronic temperature is shown Fig. 4.15(a).

4.8.3. Plasma-Frequency Decay: Consistency Check

We start with considering the plasma frequency which is displayed versus the electronic temperature T_{e} in Fig. 4.14(a). For delays $\tau > 0.5\,\mathrm{ps}$, it increases roughly linearly with electronic temperature. A similar rise was also observed for the plasma frequency along the c axis by electron energy loss spectroscopy [Jen91]. This behavior is typical for semimetals due to their strongly varying electronic density of states near the Fermi edge and is detailed in Fig. 4.14(b). In contrast, it does not occur in metals with their rather constant eDOS as already mentioned in Section 1.6.1.

Figure 4.14(a) moreover shows that the slope of the measured Ω_{pl} vs. T_{e} agrees well with a theoretical prediction based on Eq. (1.22) and the SWM band structure. The absolute values deviate from those measured by less than 10 %. This agreement demonstrates the consistency of our fit results. For delays $\tau < 0.5\,\mathrm{ps}$, Ω_{pl} vs. T_{e} clearly leaves the linear trend. This finding indicates that the electrons have not sufficiently thermalized at this early stage after excitation as also seen in experiments employing TRPES [Moo01].

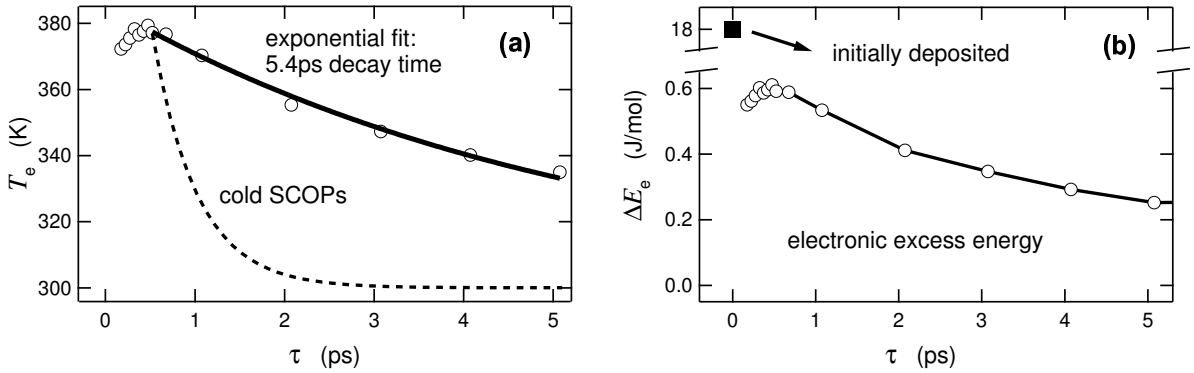

Figure 4.15.: (a) Temporal evolution of the electronic temperature T_e. The dashed line indicates the hypothetical T_e decay if only *cold* SCOPs were involved; the solid line marks an exponential decay with a time constant of 5.4 ps. (b) Temporal evolution of the pump-induced excess energy ΔE_e of the electrons. Note that the initially deposited energy is much higher than that measured for delays $\tau > 0.5$ ps.

4.8.4. Temperature Decay: Ultrafast Generation of Few Optical Phonon Modes

The dynamics of the electronic temperature T_e is shown in Fig. 4.15(a) for $\tau > 0.5$ ps since, according to the preceding section, the temperature concept does not make sense for earlier delays. T_e vs. τ follows an exponential decay with a 5.4-ps time constant.

Ultrafast Phonon Heating

T_e can be converted into the pump-induced excess energy of the electrons by

$$\Delta E_e = \int_{T_{e\infty}}^{T_e} \mathrm{d}T\, C_e(T)$$

where the electronic heat capacity C_e used has been determined via the theoretical eDOS of graphite [Nih03]. Fig. 4.15(b) shows the temporal decay of the electronic excess energy ΔE_e featuring a remarkable result: Although the entire absorbed pump-pulse energy is initially deposited in the electron system, more than 90 % (!) of this energy has left the electron system already 0.5 ps after sample excitation.

Only heat transfer to the graphite lattice can explain this finding, since, in contrast to other time-resolved experiments [Moo01], ultrafast transport does not occur in our thin and homogeneously excited sample. As mentioned in Section 4.4, electrons in graphite are solely scattered by phonons which have their wavevector component $\boldsymbol{q}_\perp$ close to the Γ or K point of the Brillouin zone. Therefore, only a quite restricted phonon subset can directly dissipate the electronic energy and heats up. These hot phonons cool down by heat transfer to cold lattice modes via ph-ph coupling on a much longer time scale of ~ 10 ps.

The latter time scale is suggested by the decay time of coherent lattice vibrations which can be generated by a short laser pulse [Mis00]. In this way, the hot phonons dictate the observed slow decay of T_e with a time constant of 5.4 ps in Fig. 4.15(a).

The maximum temperature increase of the hot phonons can be estimated from the absorbed laser fluence as follows: Figure 4.6(b) shows that electrons of higher energy $\epsilon - \epsilon_F$ will emit or absorb phonons with a larger wavevector

$$|\Delta \boldsymbol{k}_\perp| \approx \frac{|\epsilon - \epsilon_F|}{\gamma_0}$$

where $\gamma_0 \approx 3\,\text{eV}$ is the slope of the graphene bands. When we set the electron energy to half the pump photon energy, $|\epsilon - \epsilon_F| = \hbar\omega_{pump}/2 \approx 0.8\,\text{eV}$, we obtain an upper limit of $|\Delta \boldsymbol{k}_\perp|$ that corresponds to $\sim 10^{-1}$ of the diameter of the hexagonal BZ. Therefore, only $\sim 10^{-2}$ of all phonon wavevectors directly interact with the electrons. Accordingly, the heat capacity of the hot phonons is that of graphite reduced by the same factor. Therefore, the maximum temperature increase of the hot phonons is $\sim 10^2 \cdot \Delta T \sim 100\,\text{K}$ where $\Delta T \approx 3\,\text{K}$ is the expected final temperature increase of the excited graphite, see Eq. (4.12).

This estimate is in good agreement with the experimental data in Fig. 4.15(a). Thus, our measurements reflect the ultrafast generation of hot phonons and their subsequent slow cooling.

SCOPs Dominate the Energy Transfer

As seen above, the phonons cool the laser-excited electrons within 0.5 ps although only $\sim 10^{-2}$ of all phonon wavevectors directly take part in this process.

We now show that the SCOPs dominate the energy loss of the electrons by employing the following gedankenexperiment: Since cold phonons result in a faster electron cooling than hot phonons, we first assume the SCOPs to be *cold* and the only lattice modes interacting with the electrons. We use the 2-temperature model of Section 1.3.2 and the theoretical matrix elements of e-ph coupling in graphite to calculate the temporal decay of T_e; technical details are described in Appendix C.2. With a fixed phonon temperature of 300 K and an initial electronic temperature of 380 K at $\tau = 0.5\,\text{ps}$, we obtain the dashed curve in Fig. 4.15(a). Note that this hypothetical decay is much faster than that measured. Therefore the assumption of cold SCOPs at $\tau = 0.5\,\text{ps}$ has to be wrong, and we have found further evidence for ultrafast phonon heating. It should be noted that other Γ and K phonons in graphite lead to similar decay curves only if comparable or even larger e-ph matrix elements are assumed, which is in contradiction to theoretical results [Pis04].

In summary, the electron cooling within only few 100 fs is dominated by the generation of hot SCOPs. It proceeds significantly faster than in doped semiconductors [Els89, Pel98] as a consequence of the strong e-ph coupling and the large phonon quantum energies of up to 0.2 eV. Metals also can dissipate the electronic energy quickly but this is due to their large Fermi surface which involves the generation of all phonon wavevectors. The slow decay of T_e back to 300 K provides an estimate of the SCOP lifetime of 5.4 ps.

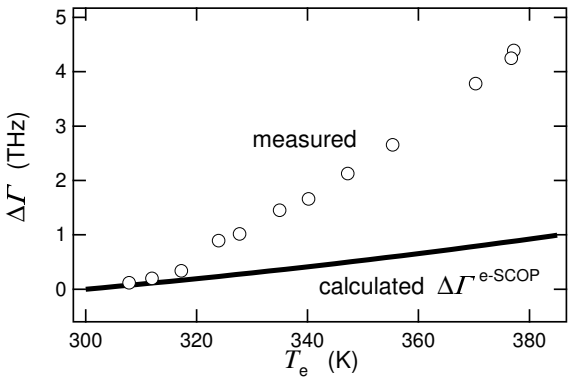

Figure 4.16.: Pump-induced changes $\Delta\Gamma$ in the Drude scattering rate (○) vs. electronic temperature T_e. Velocity relaxation of the electrons due to scattering with the SCOPs can explain a significant part of the observed striking increase of $\Delta\Gamma$ as shown by the calculated $\Delta\Gamma^{\text{e-SCOP}}$.

4.8.5. Drude Scattering Rate

While $\partial T_\text{e}/\partial\tau$ is a measure of electronic energy relaxation, the classical Drude rate Γ quantifies the decay of an electronic current when the driving electric field is switched off, see Section 1.5.1. In Fig. 4.16, Γ shows a remarkable increase from $\Gamma_\infty = 10\,\text{THz}$ by more than 3 THz, although T_e has increased by less than 80 K. This is in contrast to comparable measurements on n-doped InAs where similar electronic temperatures but an order of magnitude smaller effect on Γ were found [Els89].

What processes cause this significantly different behavior in graphite? As detailed in Section 1.6, the Drude absorption is due to IOTs which require some wavevector source. Among these, phonons are more sensitive to temperature changes than impurities. We calculate the contribution of the SCOPs to the increase of Γ with electronic temperature T_e by using Eq. (1.24), the SWM band structure (4.4), and the e-ph matrix elements from DFT calculations [Pis04]. Moreover, the SCOP occupation numbers are assumed to follow the Bose-Einstein distribution (1.5) at a temperature that equals the instantaneous electronic temperature T_e. Computational details are described in Appendix C.3. The result of this calculation is shown in Fig. 4.16. It demonstrates that the hot optical phonons can explain about 25 % of the observed increase of the current relaxation rate although their occupation numbers are still small at 380 K. The reason is mainly the strong coupling between SCOPs and electrons. Dominating contributions to $\Delta\Gamma$ by other phonons near Γ and K are not expected, since they are only weakly coupled to the electronic system [Pis04].

The question arises why the measured $\Delta\Gamma$ is even larger than the calculated SCOP contribution.

1. The theoretical curve in Fig. 4.16 should be considered as a lower limit of the true contribution $\Delta\Gamma^{\text{e-SCOP}}$ of the SCOPs to $\Delta\Gamma$ since the theory used is expected to underestimate the current relaxation. As discussed in Section 1.7, it does not account for IOTs where the photon changes the electron Bloch state. However, in graphite, resonant intermediate states in other bands can make additional contributions [Dum61]. Furthermore, IOTs involving more than 1 phonon are not accounted for.

2. As mentioned in Section 1.7, electron-electron (e-e) scattering is suggested to be quite effective in graphite. Assuming that the contribution of e-e scattering is the remaining contribution to the observed $\Delta\Gamma = \Delta\Gamma^{\text{e-SCOP}} + \Delta\Gamma^{\text{e-e}}$ and using [Mal79, Kav84]

$$\Gamma^{\text{e-e}} = AT_{\text{e}}^2$$

one obtains $A = 3.7 \cdot 10^7\,\text{s}^{-1}\,\text{K}^{-2}$. This value is about 1 order of magnitude larger than those reported for noble metals [Kav84] which is a reasonable result: First, e-e interaction in graphite is much less screened than in noble metals due to the lower electron density. Second and in contrast to quasifree electrons, the band structure of graphite allows to change the total band velocity of 2 colliding electrons without involving umklapp processes [Mal79, Kav84], see Section 1.7. In contrast, n-doped InAs exhibits only 1 parabolic band around ϵ_{F} and shows a much smaller increase of the Drude scattering rate under excitation conditions similar to our experiment [Els89]. Thus, our results are consistent with strong e-e scattering as a further source of current relaxation in graphite.

4.9. Conclusion and Outlook

The ultrafast dynamics of optically excited charge carriers in graphite have been investigated by time-resolved THz spectroscopy. We find an ultrafast energy transfer from the excited electrons to only *few* strongly coupled optical phonon (SCOP) modes within 0.5 ps. The decay of the resulting nonequilibrium population of hot phonons provides an estimate for the lifetime of these vibrational modes of 5.4 ps. Their occurence was not considered in previous reports on carbon nanotubes where a fast and slow decay of the measured signal was assigned to e-e and e-ph coupling, respectively [Her00, Zam05]. Our work, however, underlines the importance of hot optical phonons which also contribute significantly to the striking increase of the Drude scattering rate. Therefore, they might limit the performance of carbon nanotubes circuits not only at high electric fields [Jav04], but also at elevated temperatures and high frequencies. We expect the electronic energy relaxation by those strongly coupled optical phonons to play an important role also in other areas like phonon-mediated surface chemistry [Bon99]. The selective excitation of only few phonon modes may influence the desorption dynamics and products remarkably.

Future experiments will involve the amplified laser system to measure the THz response of graphite at much higher pump fluences. It is an interesting question how the electron dynamics changes close to the melting point [Mal86].

A possible experiment to isolate the significance of e-e scattering in the velocity relaxation would employ a sample of n-doped graphite with completely filled π^* valence bands. Then electrons from bands of only positive curvature should be involved in an e-e collision, and the total electron velocity should change much less than in undoped graphite.